



A Comprehensive Parametric Analysis of Geometric Effects on the Natural Frequencies of Auxetic and Honeycomb Beams

S. M. R. Khalili^{a,*}, J. Lotfi^a, P. Mahajan^b

^a Center of Research for Composite and Smart Materials and Structures, Faculty of Mechanical Engineering, K.N. Toosi University of Technology, Tehran, Iran

^b Department of Applied Mechanics, Indian Institute of Technology- Delhi, New Delhi, India

Abstract

This paper Presents a comprehensive finite element method (FEM) study of the free vibration behavior of auxetic and honeycomb beams, using Euler–Bernoulli beam theory (EBBT). For the first time, a systematic parametric analysis is conducted to investigate the impact of unit cell (UC) geometry, including connection angle, link length, and thickness, on the natural frequency of both beam types by considering more than 22,000 different UC geometries. In this regard, a novel and adjustable UC design is employed to directly compare the auxetic and honeycomb configurations. The study also explores the influence of UC row numbers and orientations on the natural frequency of these beams. The results declare that variations in each of them lead to nonlinear increases or decreases in natural frequencies. As well, for most cases under identical conditions, the natural frequencies for honeycomb beams are found to be higher than those for auxetic beams. These findings address a significant gap in the literature and provide valuable insights for the design of lightweight, vibration-resistant structures in applications such as aerospace, automotive, and smart systems. Furthermore, this work contributes to the advancement of parametric design in auxetic and honeycomb beams, offering a framework to support dynamic and vibration performance improvements in engineering applications.

Keywords: Free vibration, Auxetic beam, Euler-Bernoulli beam theory, Finite element method, Natural frequency, Honeycomb beam

1. Introduction

Lattice beams, such as honeycomb beams (positive Poisson's ratio) and auxetic beams (negative Poisson's ratio) have been employed in a great many structures and buildings due to their extraordinary properties such as high specific stiffness, lightweight, reliable flexural properties, and acceptable energy absorption capability [1-9]. In the aerospace industry, these lattice beams are integral to components such as engine vanes, thermal protection systems, aircraft nose cones, and wing panels. Honeycomb and auxetic beams diminish weight while keeping structural integrity under

* Corresponding Author Tel: (+98 21) 8406 3208; fax: (+98 21) 8867 7274.
E-mail address: smrkhalili2022@gmail.com.

aerodynamic and thermal loads, thereby enhancing fuel efficiency and performance [10]. Additionally, these beams function as vibration absorbers, modifying dynamic stresses in aircraft and spacecraft. In automotive applications, they are incorporated into bumpers, cushions, thermal protection components, sound and vibration absorbers, and fasteners, offering lightweight solutions with high impact resistance and noise reduction capabilities [1, 2]. In mechanical engineering, auxetic and honeycomb beams also demonstrate superior energy absorption and are essential in the design of lightweight components [11-13].

Both auxetic and honeycomb beams are made from the simplest repeating parts that are named unit cells (UCs). Furthermore, UCs play a vital role in the mechanical properties of lattice beams such as Young and shear moduli [14-18]. For instance, Bodaghi et al. [19] studied reversible energy absorption of 3D printed polymer auxetic structure under static compressive load. They found that auxetic structures can be used in energy absorbing application. Finally, they proposed a FE method to model the experimental test. Rezaei et al. [20] optimized some types of auxetic lattice structures to develop efficient designs with negative Poisson's ratios, aiming to enhance mechanical performance. They also experimentally investigated potential instabilities, such as buckling, in the designed structures. Lotfi et al. [21] conducted a comprehensive study on honeycomb and auxetic UCs by analyzing both micro-mechanics and macro-mechanics. The results demonstrated that when the angle between the links (connection angle) in both auxetic and honeycomb UCs exceeds 18° , Young's modulus in the X direction is consistently smaller than in the Z direction. Additionally, they revealed that regardless of the dimensions of the UCs, the auxetic UC is softer in the Z direction and stiffer in the X direction compared to the honeycomb UC. Furthermore, the honeycomb UC exhibits a higher shear modulus than the auxetic one. Bora et al. [22] presented a mathematical solution to establish the relationship between elastic properties, such as Poisson's ratio, and the geometry of the UC. Their results discovered that an increase in the connection angle leads to higher stiffness. Additionally, the dimensions of all UC links are crucial in determining the elastic properties.

By focusing on the applications of auxetic and honeycomb beams highlighted earlier the determination of the natural frequencies (when external forces are zero) of these beams is important. In a critical state, resonance can occur when the frequency of dynamic loads (including wind and earthquakes) matches one of the beam's natural frequencies. This phenomenon can lead to excessive vibrations, potentially resulting in structural collapse [23, 24]. In this context, Şakar et al. [25] studied the natural frequencies for honeycomb beams both numerically and experimentally. The study revealed that reducing either the unit cell thickness or the connection angle results in a decrease in frequency. Chen et al. [26] conducted a numerical investigation of a thin laminated plate embedded with auxetic layers subjected to dynamic loads. Euler–Bernoulli beam theory (EBBT) was employed to derive formulation and determine the natural frequencies. It was observed that the natural frequency values decrease nonlinearly as the absolute value of Poisson's ratio approaches zero. Zamani et al. [27] proposed a novel design for auxetic UCs and presented an exact solution for determining their elastic properties. Dynamic analysis revealed that incorporating these UCs as the core of sandwich structures significantly increased their natural frequencies. Furthermore, the results demonstrated that using the proposed UCs as the core, enhanced the specific modulus (stiffness-to-weight ratio) of the sandwich structure. Kushwaha et al. [28] investigated numerically the first three natural frequencies of a few lattice beams including both auxetic and honeycomb beams. Their findings showed that the honeycomb beam had higher 1st and 3rd natural frequencies compared to the auxetic beam. Jiang et al. [29] presented both analytical and numerical (FEM) models to determine the natural frequencies of composite auxetic sandwich plates. They concluded that, for sandwich plates of equal weight, the natural frequencies increased by raising both the connection angle and UC thickness. Finally, the results were validated using experimental data. Hosseini et al. [30] investigated the influence of a limited number of auxetic cores on the natural frequency of 3D-printed sandwich beams. Their findings indicated that increasing the connection angle led to an increase in the natural frequency. Quan et al. [31] proposed an analytical solution to accurately calculate the natural frequency of sandwich plates with a honeycomb core. The study employed the First-Order Shear Deformation Theory (FSDT), assuming small deformations and small rotations, to derive the strain field. It was also supposed that the sandwich plate was supported by Winkler-Pasternak elastic foundations. The results showed that the natural frequencies diminished when either the connection angle or the link length-to-thickness ratio was reduced.

A review of the existing literature reveals that only a limited number of studies have investigated the influence of UC geometry on the natural frequencies of auxetic and honeycomb beams. Furthermore, these studies typically examine only a few discrete configurations, often focusing exclusively on either the connection angle or the link length, without conducting a comprehensive analysis of their combined effects [25, 28, 30, 31]. This indicates a significant research gap and emphasizes the necessity for more systematic and parametric investigations in this field. Addressing this gap is particularly crucial, as understanding the vibrational behavior and natural frequencies of auxetic and honeycomb beams is essential for optimizing their dynamic performance and ensuring structural reliability. These core structures are extensively utilized in aerospace, mechanical, and civil engineering applications. For instance, they are used in lightweight, high-performance aircraft wings and vibration-damping systems for bridges, due to their

superior mechanical properties mentioned earlier [14, 16]. In response to this identified gap, the present study employs a novel and adjustable UC design to enable a direct and consistent comparison between auxetic and honeycomb beam configurations. For the first time, a comprehensive and systematic parametric analysis is conducted, simultaneously investigating the influence of all major geometric parameters, including connection angle, link length, and link thickness, across a wide range of both UC types. Additionally, the effects of the number and orientation of UC rows and columns on the natural frequencies are explored. To achieve this, a dynamic finite element model based on energy methods and Euler–Bernoulli beam theory is employed. Natural frequencies are calculated by solving the eigenvalue problem using a robust program developed on the standard version of MATLAB®, and the results are validated against exact solutions of Euler–Bernoulli beams (EBB). The results, including trends in the natural frequency and the frequency ratio between honeycomb and auxetic beams, are illustrated using detailed contour plots and response curves. Through this approach, the study effectively addresses the existing research gap and offers valuable insights for the dynamic optimization of auxetic and honeycomb beam structures.

2. Modelling

2.1. Geometrical design

Lattice beams, such as auxetic and honeycomb beams with negative and positive Poisson's ratios respectively, are constructed from the simplest repeating unit cells (UCs), where the members are modeled as beam elements [15]. Therefore, it is essential to begin by providing a clear definition of the UC for both auxetic and honeycomb beams, based on data from the literature. Bodaghi [15, 19, 32], and Ahsan [33] separately presented the UC for auxetic and honeycomb beams. However, as shown in Fig. 1, Lotfi [21] introduced innovative UCs with only three links for both auxetic and honeycomb configurations, which can be transformed into one another by altering the connection angle (β). These UCs are selected to construct lattice beams in the present work.

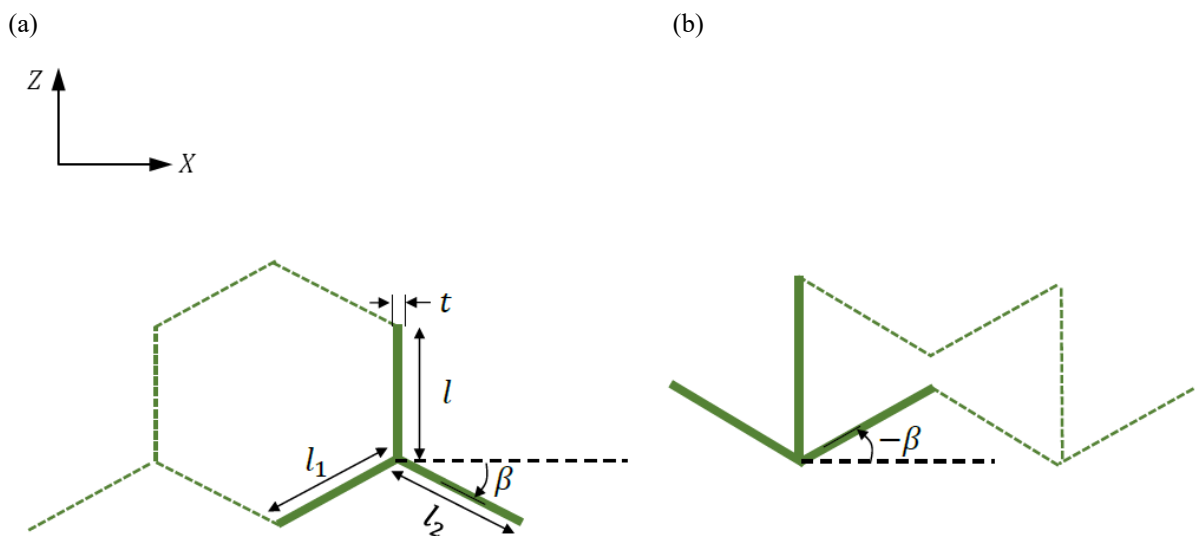


Fig. 1. Geometry and dimensions of (a) honeycomb unit cell, and (b) auxetic unit cell with only 3 links (Marked with solid lines) and a connection angle (β).

In the selected UCs, l_1 equals l_2 , reducing the parameters to be defined to two link lengths and the value of β . Therefore, to supply a comprehensive numerical study, the non-dimensional parameter is defined as follows:

$$\psi = \frac{l_1}{l} \quad (1a)$$

$$\chi = \frac{l}{t} \quad (1b)$$

2.2. FE formulation

The EBBT can be regarded as a specific case of the general beam theory (finite strain beam theory), applicable when the beam is sufficiently long and slender. This ensures that the effects of shear deformations are typically negligible [34, 35]. In simpler terms, the beam's length-to-thickness ratio must be sufficiently large for the assumptions of EBBT to hold valid [36]. Hence, Fig. 2 illustrates the EBB element, characterized by a length l , thickness h , and width b , as well as represented with two nodes. The coordinate system (X, Y, Z) is fixed at the mid-left of the beam element to provide a consistent reference frame. Based on the assumptions of both small axial and small transverse displacements (u, w) and small rotation (θ) , the displacement vector (\mathbf{U}) can be described as follows [36]:

$$\mathbf{U} = \begin{Bmatrix} Z\theta + u(X) \\ 0 \\ w(X) \end{Bmatrix} \tag{2}$$

where $\theta = -\frac{\partial w(X)}{\partial X}$

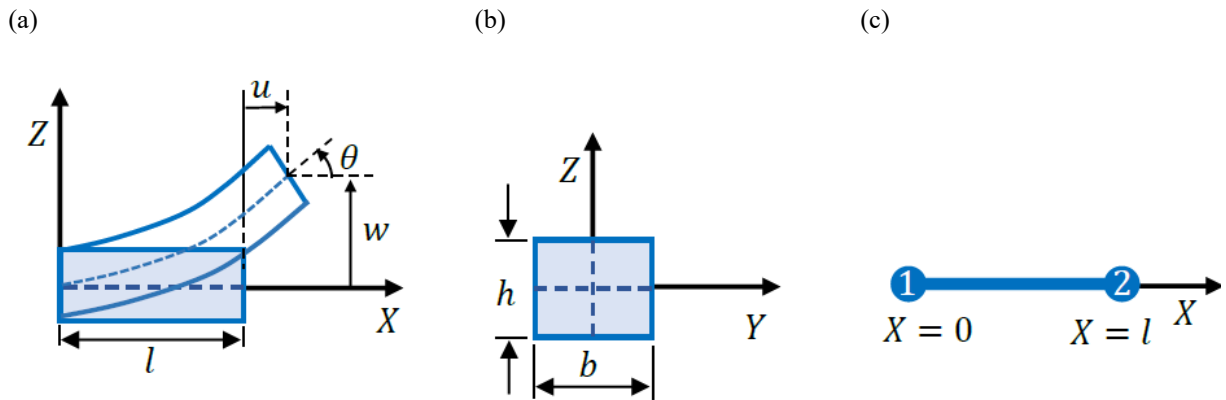


Fig. 2. Coordinate systems and a standard beam element, (a) deformed beam element, (b) the geometry of cross-section, and (c) typical 2-node beam element.

Based on Eq. (2), and assuming the lattice beam material to behave as a homogeneous, isotropic, and linearly elastic solid, the strain energy can be defined as [36]:

$$W = \frac{1}{2} \int_0^l E \left(A \left(\frac{\partial u}{\partial X} \right)^2 + I \left(\frac{\partial^2 w}{\partial X^2} \right)^2 \right) dX \tag{3}$$

where E indicates Young's modulus, while A , and I denote, the area and the second moment of area that can be determined for the beam shown in Fig. 2b as:

$$A = bh \tag{4a}$$

$$I = \frac{1}{12}bh^3 \tag{4b}$$

It is also evident that strain energy can be divided into two distinct components, axial energy, and bending energy, which are associated with axial stiffness (EA) and bending stiffness (EI) , respectively (Further information is available in [37, 38]). Moreover, the kinetic energy of an EBB is:

$$T = \frac{1}{2} \int_0^l \rho (A(\dot{u}^2 + \dot{w}^2) + I\dot{\theta}^2) dX \quad (5)$$

where ρ denotes density and a superposed dot (.) indicates time derivative. By employing Equation (2), it can be seen that $\dot{\theta} = \left(-\frac{\partial \dot{w}(X)}{\partial X}\right)$ thus confirming that the effects of rotary inertia is neglected, consistent with EBBT. Considering an EBB as depicted in Fig. 2c with two nodes located at $X = 0$ and $X = l$, the FE formulation is subsequently employed. The displacement functions (u, w) are obtained by employing linear and cubic polynomial shape functions, respectively as [39]:

$$u = [N_{1u} \quad N_{2u}] \begin{bmatrix} u_1 \\ u_2 \end{bmatrix} \quad (6a)$$

$$w = [N_{1w} \quad N_{2w} \quad N_{3w} \quad N_{4w}] \begin{bmatrix} w_1 \\ \theta_1 \\ w_2 \\ \theta_2 \end{bmatrix} \quad (6b)$$

where $u_i, w_i,$ and θ_i ($i = 1,2$) are nodal displacement values at the i^{th} node, while:

$$[N_{1u} \quad N_{2u}] = \left[1 - \frac{X}{l} \quad \frac{X}{l}\right] \quad (7a)$$

$$[N_{1w} \quad N_{2w} \quad N_{3w} \quad N_{4w}] = \left[1 - \frac{3X^2}{l} + \frac{2X^3}{l^3} \quad X - \frac{2X^2}{l} + \frac{X^3}{l^2} \quad \frac{3X^2}{l^2} - \frac{2X^3}{l^3} \quad -\frac{X^2}{l} + \frac{X^2}{l^2}\right] \quad (7b)$$

In the present work, Hamilton's principle, expressed in its variational form, is utilized to derive the dynamic FE governing equation as [40]:

$$\int_{t_0}^{t_1} (\delta \mathbf{\Lambda}_e \mathbf{P}_e + \delta T - \delta W) dt = 0 \quad (8)$$

where δ is the variational operator, while T and W denote the kinetic energy and strain energy of an EBB as defined in Eq. (3) and Eq. (5), respectively. Additionally, $\mathbf{\Lambda}_e$ and \mathbf{P}_e signify the total nodal displacement vector and the external forces acting on the nodes of an EBB element.

$$\mathbf{\Lambda}_e = [u_1 \quad w_1 \quad \theta_1 \quad u_2 \quad w_2 \quad \theta_2] \quad (9a)$$

$$\mathbf{P}_e = [F_1 \quad V_1 \quad M_1 \quad F_2 \quad V_2 \quad M_2] \quad (9b)$$

where $F_i, V_i,$ and M_i represent the axial force, transverse force, and bending moment, respectively, acting on the i^{th} node. Next, by substituting Eq. (3) and Eq. (5) into Eq. (8) and utilizing Eq. (6) for u and w , the dynamic FE governing equation can be obtained as:

$$\mathbf{k}_e \mathbf{\Lambda}_e + \mathbf{m}_e \ddot{\mathbf{\Lambda}}_e = \mathbf{P}_e \quad (10)$$

where \mathbf{k}_e and \mathbf{m}_e are the stiffness matrix and mass matrix that is determined for each element as follows:

$$\mathbf{k}_e = \int_0^l \mathbf{\Omega}^T \mathbf{E} \mathbf{\Omega} dX \quad (11a)$$

$$\Omega = \begin{bmatrix} \frac{\partial N_{1u}}{\partial X} & 0 & 0 & \frac{\partial N_{2u}}{\partial X} & 0 & 0 \\ 0 & \frac{\partial^2 N_{1w}}{\partial X^2} & \frac{\partial^2 N_{2w}}{\partial X^2} & 0 & \frac{\partial^2 N_{3w}}{\partial X^2} & \frac{\partial^2 N_{4w}}{\partial X^2} \end{bmatrix}$$

$$E = \begin{bmatrix} EA & 0 \\ 0 & EI \end{bmatrix}$$

$$m_e = \int_0^l \rho A \Gamma^T \Gamma dX$$

$$\Gamma = \begin{bmatrix} N_{1u} & 0 & 0 & N_{2u} & 0 & 0 \\ 0 & N_{1w} & N_{2w} & 0 & N_{3w} & N_{4w} \end{bmatrix}$$
(11b)

It should be mentioned that the superposed T (T) signifies the transpose of a matrix. The stiffness and the mass of each element are derived as symmetric 6×6 matrices by evaluating the integrals in Eq. (11).

$$k_e = \frac{E}{l^3} \begin{bmatrix} Al^2 & 0 & 0 & -Al^2 & 0 & 0 \\ 0 & 12I & 6Il & 0 & -12I & 6Il \\ 0 & 6Il & 4l^2I & 0 & -6Il & 2l^2I \\ -Al^2 & 0 & 0 & Al^2 & 0 & 0 \\ 0 & -12I & -6Il & 0 & 12I & -6Il \\ 0 & 6Il & 2l^2I & 0 & -6Il & 4l^2I \end{bmatrix}$$
(12a)

$$m_e = \frac{\rho Al}{420} \begin{bmatrix} 140 & 0 & 0 & 70 & 0 & 0 \\ 0 & 156 & 22l & 0 & 54 & -13l \\ 0 & 22l & 4l^2 & 0 & 13l & -3l^2 \\ 70 & 0 & 0 & 140 & 0 & 0 \\ 0 & 54 & 13l & 0 & 156 & -22l \\ 0 & -13l & -3l^2 & 0 & -22l & 4l^2 \end{bmatrix}$$
(12b)

In the following, the k_e and m_e matrices must be mapped to the global coordinate system. Afterward, they are assembled for the entire lattice beam, and boundary conditions are applied (details of these steps can be found in [15, 36]). By following these steps, Eq. (10) can be rewritten as:

$$K\Lambda + M\ddot{\Lambda} = P$$
(13)

where K , M , Λ , and P denote the stiffness matrix, mass matrix, nodal displacement vector, and external forces, respectively, after assembly and the application of boundary conditions. Finally, for free vibration analysis, where external forces are absent ($P = \mathbf{0}$), consider a harmonic solution of the form:

$$\Lambda = \widehat{\Lambda} e^{\sqrt{-1}\omega t}$$
(14)

where $\widehat{\Lambda}$, ω , and t signify the mode shape vector, the natural frequency, and time, respectively. Substituting Eq. (14) into Eq. (13), ω and $\widehat{\Lambda}$ are obtained by solving the following eigenvalue problem [41]:

$$(K - \omega^2 M)\widehat{\Lambda} = \mathbf{0}$$
(15)

It is important to highlight that all calculations are performed using a robust program developed on a personal computer (PC) with the home version of MATLAB®.

3. Numerical results and discussion

This section begins with the verification of the proposed FE solution for determining the first five natural frequencies of the EBB and comparing it to the exact analytical solution. After verification, a parametric study is conducted on honeycomb and auxetic beams (based on the UC configuration in Fig. 1), focusing on their first natural frequency. The study examines the influence of UC geometry, including the connection angle (β) and non-dimensional parameters (ψ, χ) as defined in Eq. (1), as well as the effect of UC number and orientation. Understanding the effect of these parameters is crucial for optimizing and designing structural performance [41]. It also plays a key role in tailoring mechanical properties for engineering applications, such as aerospace and automotive. It should be emphasized that, based on the author's understanding, this parametric study addresses and fills a significant gap in the existing literature.

3.1. Verification of the Proposed FE Solution

The first five natural frequencies obtained from the proposed FE solution of the 2D beam element, by solving Eq. (15), are presented. These frequencies are then compared with the natural frequencies derived from the exact solution of EBB using the following relation [41].

$$\omega_n = \frac{\kappa_n^2}{2\pi} \sqrt{\frac{EI}{\rho AL^4}} \quad (16)$$

where E, I, ρ, A , and L represent Young's modulus, the second moment of area, the density of the beam material, the cross-sectional area of the beam, and the beam's length, respectively. Additionally, κ_n is the constant associated with the n^{th} mode shape, which can be derived from the exact solution [41]. Therefore, its corresponding values for EBBs under both clamped-free (called cantilever beam) and clamped-clamped (called simply clamped beams) boundary conditions are provided in Table 1.

Table 1. The values of κ_n (dimensionless) for clamped-free and clamped-clamped EBBs [41]

Boundary conditions	κ_1	κ_2	κ_3	κ_4	κ_5
Clamped-free	1.87	4.69	7.85	11.0	14.13
Clamped-Clamped	4.73	7.85	11.0	14.13	17.3

The required mechanical properties (E, G , and ρ) of EBB are adopted from the authors previous work, which investigated both auxetic and honeycomb structures under static conditions [21]. As discussed in the literature review, that study used 3D-printed TPU. Furthermore, to ensure compliance with EBBT assumptions, the beam's length-to-thickness ratio (L/H) is selected to be large enough. In summary, the properties of EBB are listed in Table 2.

Table 2. The EBB mechanical and geometrical properties used for exact and FE solution [21]

Mechanical/geometrical properties	E (MPa)	G (MPa)	ρ ($\frac{kg}{m^3}$)	L (mm)	b (mm)	h (mm)
Values	86.5	29	1082	100	10	2

where L, b , and h are the length, width, and thickness of the considered EBB for Verification, so $A = BH$. Table 3 presents the first five natural frequencies ($\omega_n, n = 1 - 5$) of the EBB under clamped-free and clamped-clamped boundary conditions.

Table 3. The first five natural frequencies of both clamped-free and clamped-clamped EBBs

Boundary conditions	Solution	ω_1 (Hz)	ω_2 (Hz)	ω_3 (Hz)	ω_4 (Hz)	ω_5 (Hz)
Clamped-free	FE	9.13	57.25	160.3	314.12	519.27
	Exact	9.1	57.15	160.1	314.37	518.73
Discrepancy (%)	-	0.3	0.17	0.12	0.08	0.1
Clamped-Clamped	FE	58.13	160.23	314.12	519.27	775.73
	Exact	58.13	160.1	314.37	518.73	777.58
Discrepancy (%)	-	0	0.08	0.2	0.1	0.23

As can be seen, the presented FE solution is validated through its reasonable agreement with the exact EBB solution.

3.2. Parametric study

The parametric study commences by considering general auxetic and honeycomb beams with UCs shown in Fig. 1 under a clamped-free boundary condition. The mechanical properties of all auxetic beams (A^β , $\beta < 0$) and honeycomb beams (H^β , $\beta > 0$), are defined as mentioned in Table 2 ($E = 86.5 \text{ MPa}$ and $\rho = 1082 \frac{\text{kg}}{\text{m}^3}$). Moreover, in this section, to confirm that all beams (whether A^β or H^β) are adequately long and slender (EBB), as well as to investigate the UC's geometry itself, the following conditions are considered:

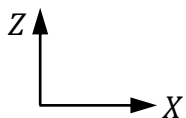
- The width of the beam (or UC) is fixed at 10 mm.
- The UC length (l , see Fig. 1) is constantly set to 5 mm ($l = 5 \text{ mm}$)
- The border thickness of the beams is equal to the UC thickness (t , see Fig. 1)
- The number of UCs is fixed at 40 along the X-axis (X direction) and only 1 row along the Z-axis (Z direction).

Additionally, to prevent physical contact between adjacent links in auxetic beams, specific geometric constraints are enforced, as outlined below.

$$l \left(\psi \cos \left(\frac{\pi}{2} - \beta \right) + \frac{1}{2} \right) > 0 \quad (17)$$

Furthermore, for better clarity, a representation of the auxetic and honeycomb beams is shown in Fig. 3. In these beams, the UC geometry is defined as $l = 5 \text{ mm}$, $\psi = 0.5$, and $\chi = 10$ for both auxetic and honeycomb beams. However, β is -12° for auxetic beams (A^{-12}) and $+12^\circ$ for honeycomb beams (H^{12}). It should be noted that these beams are meshed using beam elements, as described in Section 2.

To guarantee the accuracy and reliability of the FE solution, a mesh sensitivity analysis (mesh convergence study) is performed for the first five natural frequencies. This analysis is conducted for the beams illustrated in Fig. 3. These results are detailed in Table 4. Given these findings, it is evident that selecting 406 elements provide an optimal balance between computational cost and solution accuracy.



(a)

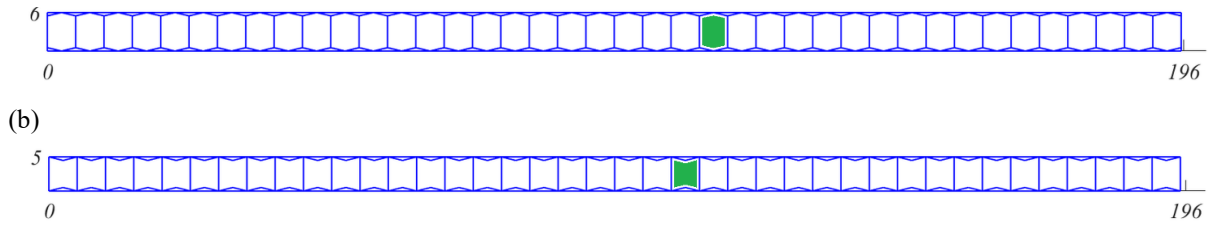


Fig. 3. Lattice beams with different types of UC; (a) honeycomb beams (H^{12}), and (b) auxetic beams (A^{-12}). In both beams $l = 5\text{mm}$, $\psi = 0.5$, and $\chi = 10$, and the number of UCs along the X-axis is set 40. Additionally, a single UC is highlighted in green and all dimensions are in mm.

Table 4. The mesh sensitivity analysis for the first five natural frequencies (ω_1 - ω_5)

Beams type	Element number	ω_1 (Hz)	ω_2 (Hz)	ω_3 (Hz)	ω_4 (Hz)	ω_5 (Hz)
H^{12}	105	7.8	31.2	65.6	102	136
	287	8.0	32.9	69.1	105.1	142.0
	406	8.06	33.36	69.72	105.38	142.06
	570	8.06	33.36	69.72	105.38	142.06
	683	8.06	33.36	69.72	105.38	142.05
	890	8.06	33.36	69.71	105.35	142.03
A^{-12}	105	6	25.4	57.52	88.5	120.12
	287	6.65	28.87	61.0	92.66	125.19
	406	6.8	29	61.23	93.24	126.15
	570	6.8	29	61.23	93.24	126.15
	683	6.8	29	61.23	93.25	126.15
	890	6.8	29	61.21	93.24	126.15

Next, the first natural frequency (ω_1) is examined over a wide range of ψ values for various beams. These include H^β with positive β values and A^β with negative β values. The present study considers a total of 150 values for ψ ($0.2 \leq \psi \leq 1.2$) and 150 values for β ($-72^\circ < \beta < 72^\circ$), resulting in 150×150 cases encompassing both A^β and H^β . Fig. 4a shows the influence of different UC geometry (ψ, β) on the ω_1 response, with χ held constant at 10 to ensure uniformity for comparison purposes. It should be mentioned that the UC geometries violating the condition specified in Eq. (17) have been omitted from Fig. 4. Notably, when either $72^\circ < \beta < 90^\circ$ or $-90^\circ < \beta < -72^\circ$, links l_1 and l_2 become very close, causing the UC to gradually transform from its original geometry. Therefore, these values of β are neglected in the present work. Upon looking at Fig. 4a, it can be observed that for all values of ψ , by increasing absolute β ($|\beta|$), ω_1 grows nonlinearly in both auxetic and honeycomb beams. This broad trend supports the results in [29, 31], where only a few cases were considered. On the other hand, according to the fundamental vibration theory, ω_1 is directly related to the square of the structure or beam stiffness. Therefore, it can be concluded that the beam's stiffness is improved by increasing $|\beta|$, this fact is consistent with [21] that investigated the stiffness of auxetic/ honeycomb UCs in a general form.

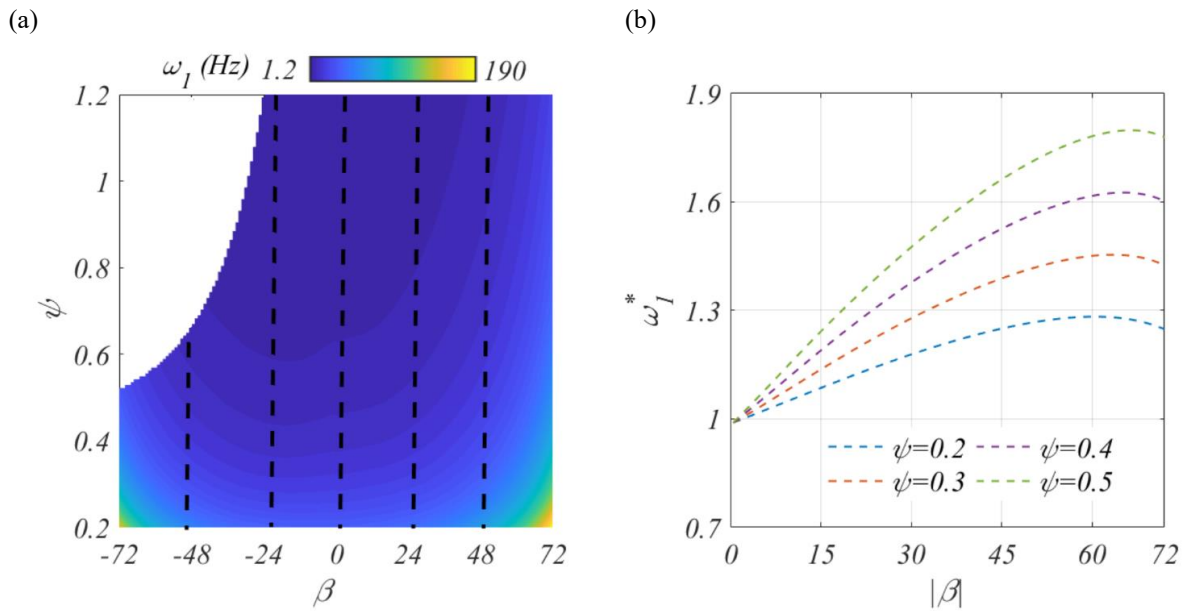


Fig. 4. The variation of (a) ω_1 in terms of β and ψ for both types of beams (A^β and H^β), and (b) the normalized ratio (ω_1^*) in terms of $|\beta|$ and some values of ψ , where $\chi = 10$.

For a more comprehensive analysis, $|\beta|$ is divided into three 24-degree intervals including $0^\circ - 24^\circ$, $24^\circ - 48^\circ$, and $48^\circ - 72^\circ$, as shown in Fig. 4. Regardless of beam type (A^β or H^β), it can be seen that the increase in ω_1 in the 3rd interval is greater than in the 1st interval. For instance, by considering $\psi = 0.2$, in the 1st interval of H^β , ω_1 experiences around 23% increase (from 35 Hz to 45 Hz), while in the 3rd interval, growth reaches about 166% (71 Hz to 189 Hz), about 7 times greater. Likewise, in A^β , the 1st interval shows only around 5% increase in ω_1 (from 35 Hz to 37 Hz), whereas the 3rd interval exhibits a growth of about 179% (from 54 Hz to 151 Hz). Although the ω_1 values are lower in A^β compared to H^β , the growth in the intervals is more pronounced in A^β . In addition, Fig. 4a reveals that not only β , but also ψ has an effect on ω_1 , a key point that fewer studies have explored. The contour plot shows that for both types of beams, and any values of β , reducing ψ leads to a nonlinear increase in ω_1 . The maximum and minimum values of ω_1 for the honeycomb beam are 189 Hz and 1.4 Hz, respectively, occurring at $(\beta = 72^\circ, \psi = 0.2)$ and $(\beta = 0.5^\circ, \psi = 1.2)$. In comparison, the corresponding values for the auxetic beam are 151 Hz and 1.2 Hz happening at $(\beta = -72^\circ, \psi = 0.2)$ and $(\beta = -23^\circ, \psi = 1.2)$. These values are approximately 1.25 and 1.16 times smaller than those for the honeycomb beam, respectively. Furthermore, the normalized ratio (ω_1^*) is another crucial parameter in designing and choosing auxetic and honeycomb beams for various applications. This is defined as the ratio of ω_1 in the honeycomb and auxetic beams when ψ and $|\beta|$ are equal for both. Undoubtedly, if $\omega_1^* > 1$, the ω_1 for the honeycomb beam with specific ψ and $|\beta|$ values will be greater than that of the auxetic beam with the same ψ and $|\beta|$, and vice versa. Fig. 4b demonstrates ω_1^* with respect to $|\beta|$ for various values of ψ (0.2, 0.3, 0.4, and 0.5), as the geometric constraint mentioned in Eq. (17). It is essential to emphasize that $\beta = 0^\circ$ is unstable, as even small changes in β can alter the sign of Poisson's ratios [21], thus in Fig. 4b, $|\beta| > 0$. It can be observed that all curves have the same trend but the maximum value of ω_1^* (1.8) occurs at $\psi = 0.5$ and $|\beta| = 66^\circ$. This indicates that the value of ω_1 for the honeycomb beam at $\psi = 0.5$ and $|\beta| = 66^\circ$ is 80% greater than that for the auxetic beam. These honeycomb and auxetic beams are shown in Figs. 5a and 5b, respectively, and a single UC is highlighted in green color. Overall, the maximum values of ω_1^* for all considered values of ψ are summarized in Table 5. It can be seen that, while the maximum values of ω_1 for both beam types occur at $\psi = 0.2$ (see Fig. 4a), switching the beam from honeycomb to auxetic results in a maximum improvement of only 28% in ω_1 (at $\beta = 60^\circ$). Furthermore, the highest value of ω_1^* is founded within the domain $60^\circ \leq \beta \leq 67^\circ$, depending on ψ , and also ω_1^* decreases if β is either increased or decreased from that domain.

Table 5. The maximum values of the normalized ratio (ω_1^*)

ψ	$ \beta $	ω_1^*
0.2	60°	1.28
0.3	64°	1.45
0.4	65°	1.6
0.5	66°	1.8

Finally, Fig. 4b reveals that only in a few beams where $\beta < 3^\circ$, the ω_1^* is less than 1, which indicates that ω_1 for the honeycomb beam is lower than that for the auxetic beam. Despite several studies [42-44] focusing just on the superiority of auxetic beam, the honeycomb and auxetic beams with $\psi = 0.2$ and $\beta = 3^\circ$ where $\omega_1^* = 1$. It can be seen that the UC of these beams is very similar.

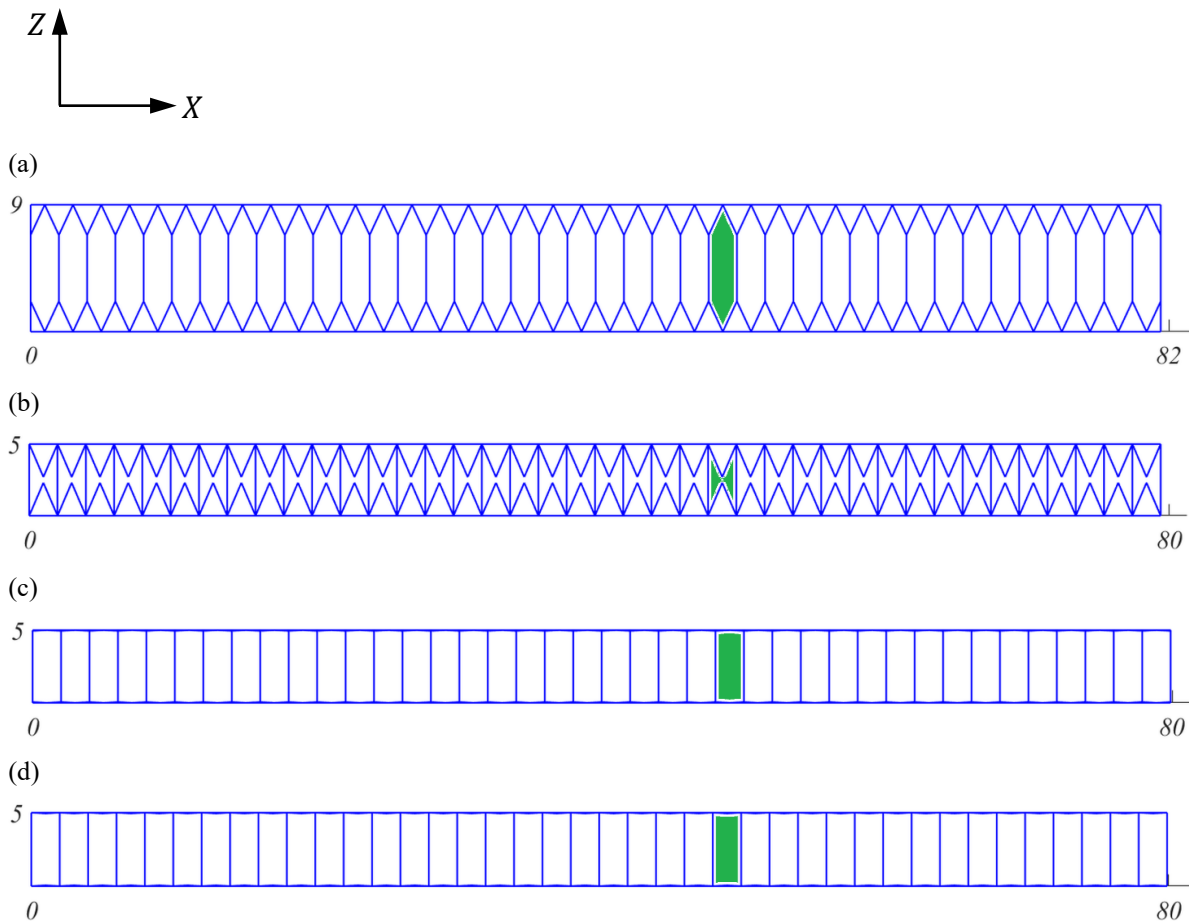


Fig. 5. Lattice beams (a) H^{66} , (b) A^{-66} with $\psi = 0.5$ which have a maximum value of $\omega_1^* = 1.8$, and (c) H^3 , (d) A^{-3} with $\psi = 0.2$ that $\omega_1^* = 1$, where $\chi = 10$. A single UC is highlighted in green and all dimensions are in mm.

Fig. 6, presents the influence of χ (Eq. (1b)), on ω_1 with $\psi = 0.5$ for both types of beams, while $|\beta| = 12^\circ$. As it can be seen, ω_1 for various χ values are denoted by different markers for both A^{-12} and H^{12} . Lagrange interpolation which involves the definition of the polynomial that passes accurately through all determined values, is employed to fit the curve to ω_1 and χ values [45]. In this context, the ω_1 is determined by solving Eq. (15) for specific χ values of both beams, after which the Lagrange interpolating polynomial ($L^*(\chi_n)$) is defined as:

$$L^*(\chi_n) = \sum_{i=0}^n (\omega_1)_i \cdot \left(\prod_{j=0, i \neq j}^n \left(\frac{\chi - \chi_i}{\chi_i - \chi_j} \right) \right) \quad (18)$$

where n is the number of χ_i and $\chi_i = [10, 15, 20, 25, 40, 50, 60, 80, 90]$. However, it can be observed that for all considered values of χ , the ω_1 for the honeycomb beam is greater than that for the auxetic beam. This is a noteworthy result, indicating that the effect of thickness cannot neutralize the other geometric impacts (ψ and β). Furthermore, the smallest discrepancy between the beams is only 0.2 Hz and happens at $\chi = 90$. It is also evident that the ω_1 values for both beams exhibit a nonlinear decrease as χ increases. Finally, by summarizing Figs. 4-6, it is highlighted that the results found from the parametric study are of utmost importance for the design of both auxetic and honeycomb beams (or structures). These results have to be investigated and optimized for each specific engineering application.

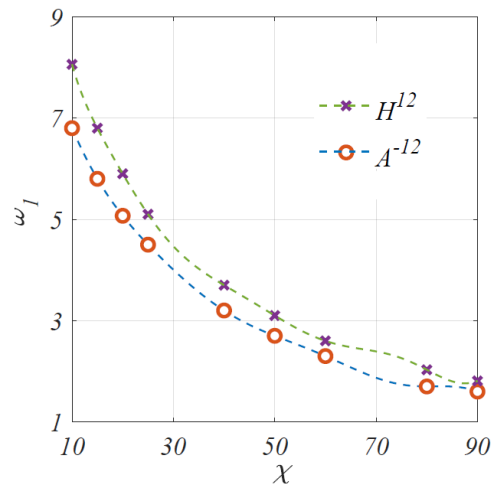


Fig. 6. The effect of χ on ω_1 for H^{12} and A^{-12} , where $\psi = 0.5$.

3.3. UC number and their orientation

In this section, the study of the first natural frequency for both auxetic and honeycomb beams is developed. The effect of the number of UC rows along the Z direction (Z-axis) and their orientation is investigated separately under a clamped-free boundary condition with mechanical properties that are provided in Table 2.

Fig. 7 displays the effect of the number of UC rows in the Z direction (N_z) for both auxetic and honeycomb beams in which the UC geometry is $l = 5\text{mm}$, $\psi = 0.5$, $|\beta| = 12^\circ$, and $\chi = 10$, also the beam's width is fixed on 10mm . It should be emphasized that the number of UCs in the X direction has been extended to 80, thus confirming that the beams (whether H^{12} or A^{-12}) remain long, and the assumptions of the EBBT still hold valid. At first glance, Fig. 7 shows that ω_1 increases for both H^{12} and A^{-12} when an additional row is added in the Z direction, signifying that the beam becomes stiffer. It can also be observed that the intensity of the ω_1 increase is highest at first, gradually decreasing with higher rows. Specifically, for H^{12} , adding the 2nd row increases ω_1 by approximately 103% (from 2.23 Hz to 4.54 Hz). In contrast, for the H^{12} with four rows, ω_1 increases by about 18% (from 6.1 Hz to 7.2 Hz) compared to the beam with three rows. Likewise, for the A^{-12} , the addition of the 2nd row increases ω_1 by roughly 100% (from 1.85 Hz to 3.7 Hz). However, changing from three rows to four rows results in an 18% increase in ω_1 (from 5 Hz to 5.9 Hz). In conclusion, the trend of increasing ω_1 is approximately the same for both types of beams. From a comparative viewpoint, the values of ω_1 for A^{-12} are consistently smaller than those for H^{12} when the number of UC rows in the Z direction is equal. This result is a general development from the previous section's outcomes, which considered only one row. However, it is evident that this result may be violated in some cases with unequal rows. For instance, the value of ω_1 for A^{-12} with two rows is approximately 66% more than ω_1 value for H^{12} with only one row.

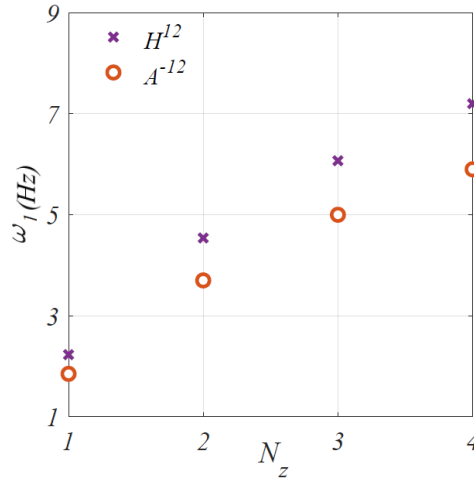


Fig. 7. The effect of the number of UC rows along the Z direction (N_z) on ω_1 for H^{12} and A^{-12} , where $l = 5\text{mm}$, $\psi = 0.5$, $|\beta| = 12^\circ$, $\chi = 10$, and 80 UCs along X direction.

In addition to the geometry and number of UCs, their orientation is also crucial in the mechanical properties of lattice beams (or structures). It is important to note that the details regarding the orientation of the UCs in lattice beams can be found in [21, 46]. In the present work, a different orientation of both auxetic and honeycomb UC is investigated. These oriented UCs are created by a 90-degree rotation of both types of the presented UCs in Fig. 1 around a central point, where three links are connected. Then to compare beams with two different UC orientations, new auxetic (A_{90}^β) and honeycomb (H_{90}^β) beams with oriented UCs are defined. It should be noted that the geometric conditions are identical to those beams as shown in Fig. 3 ($l = 5\text{ mm}$, $\psi = 0.5$, $|\beta| = 12^\circ$, and $\chi = 10$) as well the width is 10 mm. As can be seen in Fig. 8, by controlling the number of UCs in the X direction (N_x), both A_{90}^{-12} and H_{90}^{-12} exhibit an approximately identical length to that of A^{-12} and H^{12} .

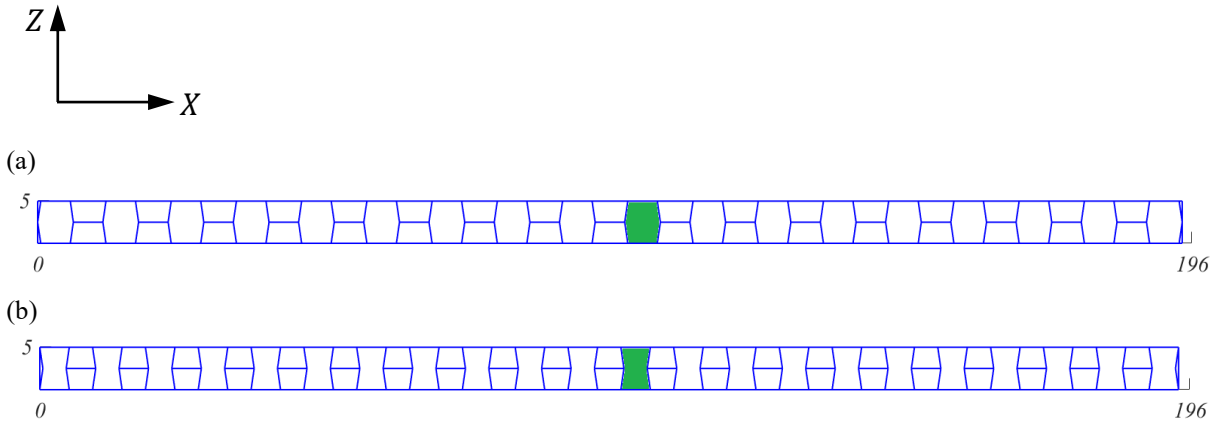


Fig. 8. Lattice beams with different types of oriented UC; (a) honeycomb beams (H_{90}^β), and (b) auxetic beams (A_{90}^β). In both beams $l = 5\text{mm}$, $\psi = 0.5$, and $\chi = 10$. Additionally, a single UC is highlighted in green and all dimensions are in mm

In the subsequent, the first five natural frequencies ($\omega_1 - \omega_5$) of these beams (A^{-12} , H^{12} , A_{90}^{-12} , H_{90}^{-12}) under clamped-free boundary conditions along with the mechanical properties listed in Table 2, are determined and given in Table 6.

Table 6. The first five natural frequencies for A^{-12} , H^{12} , A_{90}^{-12} , H_{90}^{-12}

N_x	L (mm)	H (mm)	ω_1 (Hz)	ω_2 (Hz)	ω_3 (Hz)	ω_4 (Hz)	ω_5 (Hz)
-------	----------	----------	-----------------	-----------------	-----------------	-----------------	-----------------

H^{12}	40	195.6	6	8.06	33.36	69.72	105.38	142.06
A^{-12}	40	195	5	6.8	29	61.23	93.24	126.15
H_{90}^{12}	18	193.7	4.9	7.4	36.5	82	129.8	178.1
A_{90}^{-12}	22	193.1	4.9	7.1	34.6	77	121.5	166.35

As shown in Table 6, whilst the beam length (L) is nearly the same across all beams, both the A_{90}^{-12} and H_{90}^{12} show remarkably lower N_x values compared to the H^{12} and A^{-12} . In other words, when the orientation of the honeycomb and auxetic UCs is rotated to 90° , N_x decreases by approximately 45% for A_{90}^{-12} and 55% for H_{90}^{12} . This is a key result for manufacturing purpose, as a smaller value of N_x reduces geometric complexity, minimizes fabrication errors, and leads to faster and more reliable production. Table 6 data exposes that in spite of [28], not only 1st and 3rd but also all of the first five natural frequencies for H^{12} are consistently higher than those for A^{-12} . Similarly, these frequencies for H_{90}^{12} are greater than those for A_{90}^{-12} . To put it another way, rotating the UCs does not result in the frequencies of A_{90}^{-12} surpassing that of H_{90}^{12} . It is worth mentioning that this trend aligns with the general pattern detected in Figs. 4a and 4b, where ω_1 is investigated for H^{12} and A^{-12} . By comparing the orientations of the auxetic beams, A^{-12} and A_{90}^{-12} , it is evident that all considered natural frequencies improve in A_{90}^{-12} . The maximum and minimum improvements are approximately 32% and 4.4%, occurring for ω_5 and ω_1 , respectively. Furthermore, examining the natural frequencies for both honeycomb beam configurations (H^{12} and H_{90}^{12}) reveals that, except for ω_1 , the other frequencies are enhanced by rotating the UCs in H_{90}^{12} . As previously mentioned, the natural frequency is directly related to the stiffness-to-weight ratio, which is a critical parameter in mechanical engineering. Finally, it is observed that the values of variation in natural frequencies, whether increasing or decreasing, are nonlinear for both types of beams and orientations. Therefore, the study of free vibrations in auxetic and honeycomb beams demands considerable attention.

4. Conclusions

In this paper, a comprehensive FEM study of the free vibration behavior of auxetic and honeycomb beams based on EBBT was presented. The governing equation for free vibration was derived by employing Hamilton's principle, and the natural frequencies were determined by solving the eigenvalue problem. Then, the first five natural frequency values of the beam under both clamped-free and clamped-clamped boundary conditions were validated through the exact solution. Furthermore, the study examined the effects of UC geometry, the number of UC rows, and UC orientation on the first natural frequency of both auxetic and honeycomb beams. This parametric analysis provides valuable insights into free vibration of these beam structures, addressing a significant gap in the existing literature. In conclusion, the key findings are as follows:

- 1- By considering a wide range of connection angles ($-72^\circ \leq \beta \leq 72^\circ$) and length ratios ($0.2 \leq \psi \leq 1.2$), it can be observed that both increasing $|\beta|$ and reducing ψ caused the omega to increase nonlinearly in both auxetic and honeycomb beams.
- 2- The maximum values of the ω_1 in the honeycomb and auxetic beams were 189 Hz and 151 Hz, happening at ($\beta = 72^\circ, \psi = 0.2$) and ($\beta = -72^\circ, \psi = 0.2$), respectively.
- 3- In most cases, for identical UC geometries, the ω_1 for honeycomb beams was greater than that for auxetic beams. The maximum discrepancy was observed at $\psi = 0.5$ and $|\beta| = 66^\circ$, where ω_1 for the honeycomb beam was 80% greater.
- 4- For both honeycomb and auxetic beams, decreasing UC thickness (or increasing $\chi = \frac{l}{t}$) resulted in a gradual decrease in ω_1 values.
- 5- The value of ω_1 increased with the addition of rows to both honeycomb and auxetic beams. However, the effect of adding a second row was significantly more obvious than adding a third row.

- 6- The use of oriented UCs, created by a 90-degree rotation, did not cause the auxetic beams to surpass the honeycomb beams in frequency.
- 7- In most cases, the first five natural frequencies were enhanced by using oriented UCs, nonetheless, this enhancement was nonlinear, which suggests the need for a careful optimization study.

Finally, the present work offers a detailed set of results for the free vibration analysis of auxetic and honeycomb beams. These results can assist engineers in designing lightweight and vibration-resistant structures for aerospace, automotive, and smart systems by optimizing the geometry of auxetic and honeycomb beams.

References

- [1] C. Pan, Y. Han, J. Lu, Design and optimization of lattice structures: A review, *Applied Sciences*, Vol. 10, No. 18, pp. 6374, 2020.
- [2] X. Ren, R. Das, P. Tran, T. D. Ngo, Y. M. Xie, Auxetic metamaterials and structures: A review, *Smart Materials and Structures*, 2018.
- [3] M. S. Al-Khazraji, Review on impact, crushing response and applications of re-entrant core sandwich structures, *Aircraft Engineering and Aerospace Technology*, 2024.
- [4] F. Baertsch, A. Ameli, T. Mayer, Finite-Element Modeling and Optimization of 3D-Printed Auxetic Reentrant Structures with Stiffness Gradient under Low-Velocity Impact, *Journal of Engineering Mechanics*, Vol. 147, No. 7, 2021.
- [5] S. K. Bhullar, D. Rana, H. Lekeşiz, A. C. Bedeloglu, J. Ko, Y. Cho, Z. Aytac, T. Uyar, M. Jun, M. Ramalingam, Design and fabrication of auxetic PCL nanofiber membranes for biomedical applications, *Materials Science and Engineering C*, Vol. 81, 2017.
- [6] Q. Hu, G. Lu, K. M. Tse, Compressive and tensile behaviours of 3D hybrid auxetic-honeycomb lattice structures, *International Journal of Mechanical Sciences*, Vol. 263, 2024.
- [7] Z. Wang, C. Luan, G. Liao, J. Liu, X. Yao, J. Fu, Progress in auxetic mechanical metamaterials: structures, characteristics, manufacturing methods, and applications, *Advanced Engineering Materials*, Vol. 22, No. 10, pp. 2000312, 2020.
- [8] D. V. Truong, H. Nguyễn, R. Figueiro, F. Ferreira, Q. Nguyễn, Auxetic materials and structures in the automotive industry: Applications and insights, *Journal of Reinforced Plastics and Composites*, pp. 07316844251334174, 2025.
- [9] H. Mallek, H. Mellouli, M. Allouch, M. Wali, F. Dammak, Energy absorption of 3D-printed PETG and PETG/CF sandwich structures with cellular cores subjected to low-velocity impact: Experimental and numerical analysis, *Engineering Structures*, Vol. 327, pp. 119653-119653, 2025.
- [10] Y. Zhang, W. Z. Jiang, W. Jiang, X. Y. Zhang, J. Dong, Y. M. Xie, K. E. Evans, X. Ren, Recent Advances of Auxetic Metamaterials in Smart Materials and Structural Systems, *Advanced Functional Materials*, pp. 2421746, 2025.
- [11] M. Hedayatian, A. R. Daneshmehr, G. H. Liaghat, The Efficiency of Auxetic Cores in Sandwich Beams Subjected to Low-Velocity Impact, *International Journal of Applied Mechanics*, Vol. 12, No. 6, 2020.
- [12] V. Siniauskaya, H. Wang, Y. Liu, Y. Chen, M. Zhuravkov, Y. Lyu, A review on the auxetic mechanical metamaterials and their applications in the field of applied engineering, *Frontiers in Materials*, Vol. 11, pp. 1453905, 2024.
- [13] S. M. R. Khalili, S. M. A. Alavi, Computation of the homogenized linear elastic response of 2D microcellular re-entrant auxetic honeycombs based on modified strain gradient theory, *Journal of the Brazilian Society of Mechanical Sciences and Engineering*, Vol. 45, No. 1, pp. 19-19, 2022.
- [14] K. Wei, Y. Peng, Z. Qu, Y. Pei, D. Fang, A cellular metastructure incorporating coupled negative thermal expansion and negative Poisson's ratio, *International Journal of Solids and Structures*, Vol. 150, 2018.
- [15] A. R. Damanpack, M. Bodaghi, W. H. Liao, Experimentally validated multi-scale modeling of 3D printed hyper-elastic lattices, *International Journal of Non-Linear Mechanics*, Vol. 108, 2019.
- [16] J. Ma, H. Zhang, T.-U. Lee, H. Lu, Y. M. Xie, N. S. Ha, Auxetic behavior and energy absorption characteristics of a lattice structure inspired by deep-sea sponge, *Composite Structures*, Vol. 354, pp. 118835-118835, 2025.
- [17] M. Hosseini, H. Mazaheri, Mechanical behavior of graded combined auxetic-honeycomb structures, *International Journal of Mechanical Sciences*, Vol. 276, pp. 109223-109223, 2024.

- [18] B. M. M, R. M, C. Raja S, P. T. Dautre, F. Vignat, Geometric configuration and parametric evaluation of auxetic meta-materials for enhanced plastic energy dissipation in blast scenarios, *Journal of Computational Applied Mechanics*, Vol. 56, No. 1, pp. 127-144, 2025.
- [19] M. Bodaghi, A. Serjouei, A. Zolfagharian, M. Fotouhi, H. Rahman, D. Durand, Reversible energy absorbing meta-sandwiches by FDM 4D printing, *International Journal of Mechanical Sciences*, Vol. 173, 2020.
- [20] S. Rezaei, J. Kadkhodapour, R. Hamzehei, B. Taherkhani, A. P. Anaraki, S. Dariushi, Design and modeling of the 2D auxetic metamaterials with hyperelastic properties using topology optimization approach, *Photonics and Nanostructures - Fundamentals and Applications*, Vol. 43, 2021.
- [21] J. Lotfi, S. M. R. Khalili, A. R. Damanpack, Micro-Macro Analysis of Hyperelastic Auxetic Lattice Structures under Finite-Strain Regime, *International Journal of Mechanical Sciences*, pp. 109246-109246, 2024/3//, 2024.
- [22] K. M. Bora, S. K. Varshney, C. S. Kumar, Non local analytical and numerical modelling of re-entrant auxetic honeycomb, *Engineering Research Express*, Vol. 6, No. 2, pp. 025533-025533, 2024.
- [23] M. Mohammadimehr, S. V. Okhravi, S. M. Akhavan Alavi, Free vibration analysis of magneto-electro-elastic cylindrical composite panel reinforced by various distributions of CNTs with considering open and closed circuits boundary conditions based on FSDT, *JVC/Journal of Vibration and Control*, Vol. 24, No. 8, 2018.
- [24] M. Jafari, M. Mohammadimehr, Forced vibration control of Timoshenko's micro sandwich beam with CNT/GPL/CNR reinforced composites integrated by piezoelectric on Kerr's elastic foundation using MCST, *Journal of Computational Applied Mechanics*, Vol. 56, No. 1, pp. 15-42, 2025.
- [25] G. Şakar, F. Ç. Bolat, The Free Vibration Analysis of Honeycomb Sandwich Beam Using 3D and Continuum Model, *International Journal of Mechanical, Aerospace, Industrial, Mechatronic and Manufacturing Engineering*, Vol. 9, No. 6, 2015.
- [26] X. Chen, Z. Feng, Dynamic behaviour of a thin laminated plate embedded with auxetic layers subject to in-plane excitation, *Mechanics Research Communications*, Vol. 85, 2017.
- [27] M. H. Zamani, M. Heidari-Rarani, K. Torabi, A novel graded auxetic honeycomb core model for sandwich structures with increasing natural frequencies, *Journal of Sandwich Structures and Materials*, Vol. 24, No. 2, 2022.
- [28] Y. S. Kushwaha, N. S. Hemanth, N. D. Badgayan, S. K. Sahu, Free vibration analysis of PLA based auxetic metamaterial structural composite using finite element analysis, *Materials Today: Proceedings*, Vol. 56, 2022.
- [29] W. Jiang, J. Zhou, J. Liu, M. Zhang, W. Huang, Free vibration behaviours of composite sandwich plates with reentrant honeycomb cores, *Applied Mathematical Modelling*, Vol. 116, 2023.
- [30] R. Hosseini, M. Babaei, A. Naddaf, The influences of various auxetic cores on natural frequencies and forced vibration behavior of sandwich beam fabricated by 3D printer based on third -order shear deformation theory, *Journal of Computational Applied Mechanics*, Vol. 54, No. 2, 2023.
- [31] T. Q. Quan, V. M. Anh, N. D. Duc, Natural frequency analysis of sandwich plate with auxetic honeycomb core and CNTRC face sheets using analytical approach and artificial neural network, *Aerospace Science and Technology*, Vol. 144, 2024.
- [32] N. Namvar, A. Zolfagharian, F. Vakili-Tahami, M. Bodaghi, Reversible energy absorption of elasto-plastic auxetic, hexagonal, and AuxHex structures fabricated by FDM 4D printing, *Smart Materials and Structures*, Vol. 31, No. 5, 2022/5//, 2022.
- [33] A. M. M. Nazmul Ahsan, B. Khoda, Characterizing Novel Honeycomb Infill Pattern for Additive Manufacturing, *Journal of Manufacturing Science and Engineering, Transactions of the ASME*, Vol. 143, No. 2, 2021.
- [34] S. M. R. Khalili, A. R. Damanpack, N. Nemati, K. Malekzadeh, Free vibration analysis of sandwich beam carrying sprung masses, *International Journal of Mechanical Sciences*, Vol. 52, No. 12, 2010.
- [35] A. M. Ahmed, A. M. Rifai, Euler-Bernoulli and Timoshenko Beam Theories Analytical and Numerical Comprehensive Revision, *European Journal of Engineering and Technology Research*, Vol. 6, No. 7, 2021.
- [36] J. N. Reddy, 2015, *An Introduction to Nonlinear Finite Element Analysis*, 2nd Edn,
- [37] M. J. Jweeg, M. Al-Waily, K. K. Resan, *Introduction to finite element method: bar and beam applications*, in: *Energy Methods and Finite Element Techniques*, Eds., 2022.
- [38] B. Wang, J. Bai, S. Lu, W. Zuo, An open source MATLAB solver for contact finite element analysis, *Advances in Engineering Software*, Vol. 199, pp. 103798-103798, 2025.
- [39] T. Wang, J. Xu, Z. Qi, T. Zhao, Shear stress correction in Euler-Bernoulli beam theory, *Journal of Mechanical Science and Technology*, 2025.
- [40] A. R. Damanpack, M. Bodaghi, W. H. Liao, Contact/impact modeling and analysis of 4D printed shape memory polymer beams, *Smart Materials and Structures*, Vol. 29, No. 8, 2020.

- [41] S. S. Rao, Mechanical Vibrations Sixth Edition in SI Units, *Mechanical Vibrations*, 2018.
- [42] M. Wallbanks, M. F. Khan, M. Bodaghi, A. Triantaphyllou, A. Serjouei, On the design workflow of auxetic metamaterials for structural applications, *Smart Materials and Structures*, 2022.
- [43] F. Xia, Y. Durandet, P. J. Tan, D. Ruan, Three-point bending performance of sandwich panels with various types of cores, *Thin-Walled Structures*, Vol. 179, pp. 109723-109723, 2022/10//, 2022.
- [44] J. Zhang, X. Zhu, X. Yang, W. Zhang, Transient nonlinear responses of an auxetic honeycomb sandwich plate under impact loads, *International Journal of Impact Engineering*, Vol. 134, 2019.
- [45] S. C. Chapra, R. P. Canale, 2021, *Numerical Methods for Engineers, Eighth Edition*,
- [46] A. Daman Pak, J. Lotfi, S. M. R. Khalili, A Finite-Strain Simulation of 3D Printed Airless Tires, *Journal of Engineering Mechanics*, Vol. 149, No. 10, 2023/10//, 2023.